



## Supplementary Materials for

### **Quantum-State Resolved Bimolecular Collisions of Velocity-Controlled OH with NO Radicals**

Moritz Kirste, Xingan Wang, H. Christian Schewe, Gerard Meijer, Kopin Liu,  
Ad van der Avoird, Liesbeth M. C. Janssen, Koos B. Gubbels,  
Gerrit C. Groenenboom,\* Sebastiaan Y. T. van de Meerakker\*

\*To whom correspondence should be addressed.

E-mail: basvdm@science.ru.nl (S.Y.T.v.d.M.); gerritg@theochem.ru.nl (G.C.G.)

Published 23 November 2012, *Science* **338**, 1060 (2012)

DOI: 10.1126/science.1229549

#### **This PDF file includes:**

Materials and Methods  
Supplementary Text  
Figs. S1 to S3  
Tables S1 and S2  
References

# Supplementary Material

## Quantum-state resolved bimolecular collisions of velocity-controlled OH with NO radicals

Moritz Kirste,<sup>1\*</sup> Xingan Wang,<sup>1\*</sup> H. Christian Schewe,<sup>1</sup> Gerard Meijer,<sup>1</sup> Kopin Liu,<sup>2</sup>  
Ad van der Avoird,<sup>3</sup> Liesbeth M.C. Janssen,<sup>3</sup> Koos B. Gubbels,<sup>3</sup>  
Gerrit C. Groenenboom,<sup>3\*\*</sup> Sebastiaan Y.T. van de Meerakker,<sup>3,1\*\*</sup>

<sup>1</sup>Fritz-Haber-Institut der Max-Planck-Gesellschaft, Faradayweg 4-6, 14195 Berlin, Germany

<sup>2</sup>Institute of Atomic and Molecular Sciences (IAMS), Academia Sinica, Taipei, Taiwan 10617

<sup>3</sup>Radboud University Nijmegen, Institute for Molecules and Materials  
Heijendaalseweg 135, 6525 AJ Nijmegen, the Netherlands

\*Who contributed equally to this work;

\*\*To whom correspondence should be addressed;

E-mail: basvdm@science.ru.nl, gerritg@theochem.ru.nl

October 5, 2012

### **This PDF file includes:**

Supplementary text

Figs. S1 to S3

Tables S1 and S2

Full Reference List

## **1 Experimental methods**

The experiments were performed in a crossed molecular beam apparatus, which combined a 2.6 m long Stark decelerator and a 30 cm long electrostatic hexapole to manipulate the OH and

NO radical beams, respectively. The beam of OH radicals was produced via photodissociation of  $\text{HNO}_3$  seeded in Ar or Kr with a backing pressure of 1.6 bar. The velocity of the OH radicals was tuned between 200 m/s and 750 m/s using the Stark decelerator; the width of the velocity distribution at the exit of the decelerator ranged between 16 and 27 m/s (FWHM). The molecular beam of NO radicals was produced by seeding 20 % NO in Xe using backing pressure of 0.3 bar. Application of a hexapole electric field allowed the selection of the upper  $\Lambda$ -doublet component of the  $j = 1/2$  state of NO. A 2 mm diameter beamstop was installed on the molecular beam axis at the geometric center of the hexapole, and a 2 mm diameter diaphragm was positioned between the exit of the hexapole and the interaction region. Apart from effectively filtering out the Xe atoms from the beam, the beamstop-diaphragm combination had the additional advantage to greatly improve the state purity of the transmitted NO radicals. The NO package had a velocity of 310 m/s and a velocity distribution of 52 m/s (FWHM). The resulting collision energy ranged from  $70 \text{ cm}^{-1}$  to  $300 \text{ cm}^{-1}$  with a collision energy distribution of  $20 \text{ cm}^{-1}$  (FWHM).

Three pulsed dye lasers were used to detect the parent radical beams and the scattered OH radicals. The first dye laser (bandwidth  $0.06 \text{ cm}^{-1}$ ) was used to detect NO radicals via saturated laser-induced fluorescence using the  $0 - 0$  band of the NO ( $A^2\Sigma^+ \leftarrow X^2\Pi$ ) transition around 226 nm. The reagent beam of OH  $F_1(3/2f)$  radicals, as well as the OH radicals that inelastically scattered into the  $F_1(5/2e)$ ,  $F_1(7/2e)$ , and  $F_2(1/2e)$  levels, were detected with a second pulsed dye laser (bandwidth  $0.06 \text{ cm}^{-1}$ ) via saturated laser-induced fluorescence using the  $1 - 0$  band of the OH ( $A^2\Sigma^+ \leftarrow X^2\Pi$ ) transition around 282 nm. In both lasers, an energy of typically 1.5 mJ in a 8 mm diameter and 5 ns duration pulse was used. Although the bandwidths of both lasers were larger than the  $\Lambda$ -doublet splittings in the corresponding rotational levels of OH and NO, the selective detection of population in a single  $\Lambda$ -doublet level was facilitated by the parity selection rules of the electric dipole allowed (EDA) transitions, and the large energy splitting between levels of opposite parity in the  $A^2\Sigma^+$  state.

Population transfer into the  $F_1(3/2e)$  level could not be probed with a conventional pulsed dye laser, as such laser would simultaneously induce the magnetic dipole allowed (MDA) transition that probes the population in the initial  $F_1(3/2f)$  level (see Figure S1). The EDA and MDA transitions were spectroscopically separated using a pulsed dye laser system with a superior bandwidth of approximately 150 MHz. In this laser the output of a frequency stabilized single mode ring dye laser was amplified in a three stage pulsed dye amplifier pumped by a frequency-doubled injection seeded Nd:YAG pump laser. Care was taken to probe the OH populations with this narrowband laser system under unsaturated conditions (typically an energy of  $20 \mu\text{J}$  in a 8 mm diameter and 5 ns duration laser pulse was used). In Figure S1, two spectra containing the EDA and MDA transitions are shown that were recorded when the high voltage on the hexapole to manipulate the NO radical beam was switched on and off, respectively. The left two peaks correspond to the MDA transition, that are split by the hyperfine structure in the  $j = 1/2$  level of the  $A^2\Sigma^+$  state, and are seen to be unaffected by the presence of the NO radical beam. The broader feature on the right corresponds to the EDA transition, that is clearly affected by the NO radical beam. The collision induced population in the  $F_1(3/2e)$  level was inferred from the integrated intensity difference in both spectra. The minor initial population in

the  $F_1(3/2e)$  level that can be seen in Figure S1 was due to inelastic scattering of OH  $F_1(3/2f)$  radicals with background gas during the approximately 60 mm flight distance between the exit of the Stark decelerator and the center of the collision area.

All lasers had a beam diameter of 8 mm, and care was taken to shape the laser beams to produce a homogeneous intensity distribution. The experiment ran at a repetition rate of 10 Hz, and all trigger signals to synchronize the experiment were computer controlled. The voltages on the hexapole to manipulate the NO radical beam were applied only every other shot, and the collision signals were inferred from the signal intensity difference of alternating shots of the experiment. To reduce the influence of long term drifts in the experiment, the collision energy was varied in a quasi-continuous cycle. The Stark decelerator was programmed to produce a different velocity of the OH radicals every second shot of the experiment. The trigger pulses that control the NO radical beam, the hexapole, and the detection laser(s) were adjusted automatically to match the arrival time of the OH packet in the collision zone. A single cycle consisted of 12 measurements using 6 different velocities of the OH packet. In the first 6 measurements, the velocity of the OH packet was varied from high to low values; in the next 6 measurements, the OH velocity was varied from low to high velocities.

The collision induced population in the  $F_1(5/2e)$ ,  $F_1(7/2e)$ , and  $F_2(1/2e)$  levels was probed by repeating these cycles 1500 times with a fixed wavelength for the pulsed dye laser. The resulting 3000 averages were taken over a period of 10-30 days resulting in 96000 to 138000 total averages. When the  $F_1(3/2e)$  level was probed, the frequency of the narrowband pulsed dye laser was scanned over an energy interval of  $0.12 \text{ cm}^{-1}$  to cover the magnetic and electric dipole transitions. At each wavelength position, the cycle of 12 measurements was repeated 15 times, before a new wavelength position was chosen. These wavelength scans were repeated 75 to 78 times over a period of 20 to 30 days.

The fluorescence signals were recorded using dedicated data acquisition software, and were analyzed using photon counting techniques. The signal level of the parent OH packet corresponded to approximately 3000 photons per shot. The signal levels of the scattering products ranged from one photon every five shots (for the  $F_1(3/2e)$  channel) to one photon per  $\sim 100$  shots for the weakest channels. The observation of these weak signals was made possible by the excellent state purity of the Stark-decelerated beam of OH, and careful control over the stray light from the lasers.

## 2 Theoretical methods

The inelastic cross sections were computed with the coupled channels method on an energy grid of 10, 20, 30,  $\dots$ ,  $320 \text{ cm}^{-1}$ . The following Hamiltonian was used:

$$\hat{H} = -\frac{\hbar^2}{2\mu} \frac{1}{R} \frac{\partial^2}{\partial R^2} R + \frac{\hat{l}^2}{2\mu R^2} + \hat{H}_{\text{OH}} + \hat{H}_{\text{NO}} + \hat{V}_{\text{el}} + \hat{V}_{\text{disp}} + \hat{V}_{\text{ind}} + \hat{V}_{\text{rep}}, \quad (1)$$

with  $\mu$  the reduced mass of the complex,  $R$  the distance between the centers of mass of OH and NO, and  $\hat{l}$  the end-over-end orbital angular momentum operator. The monomer Hamiltonians

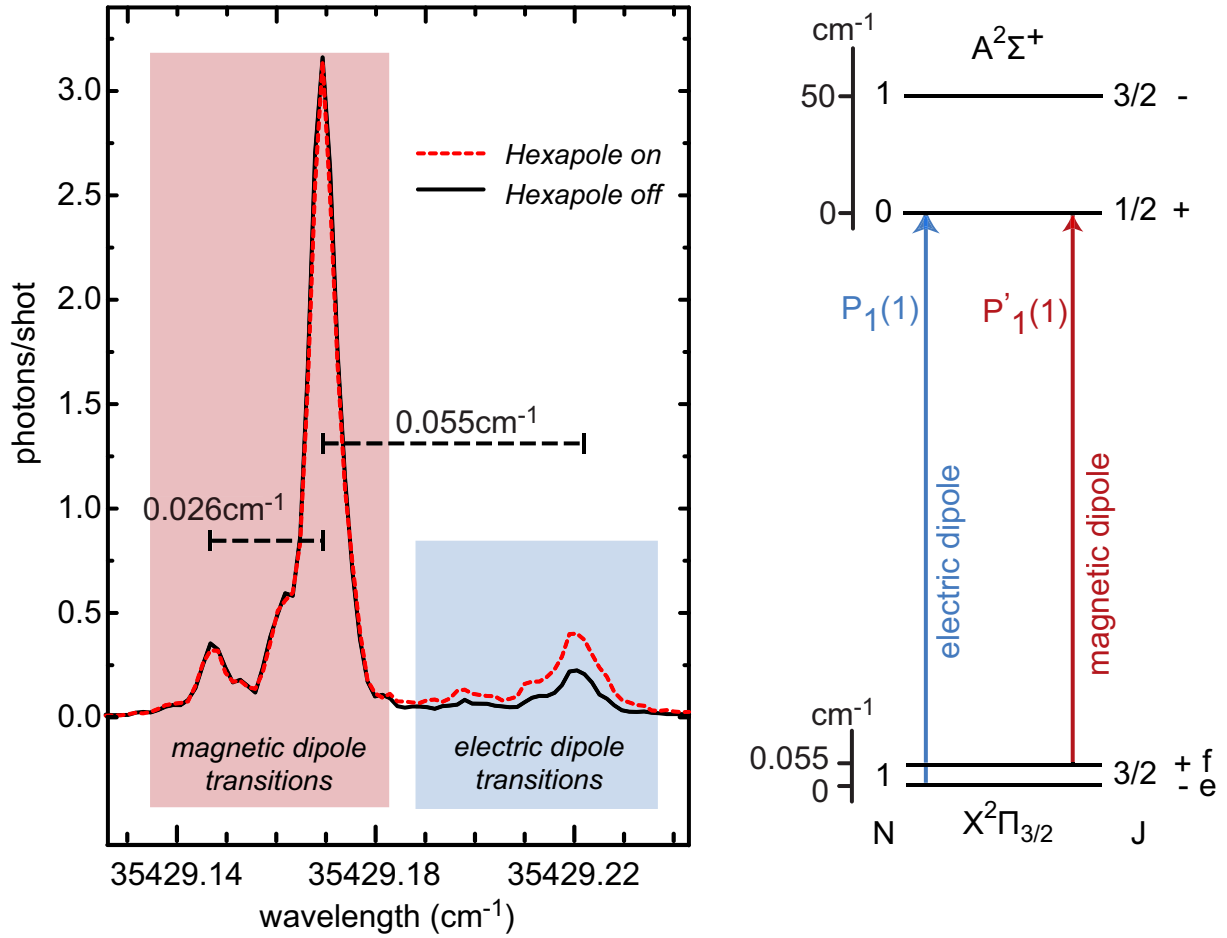


Figure S1: Magnetic dipole allowed (MDA)  $P_1(1)'$  transition that probes the population in the initial  $F_1(3/2f)$  level and the electric dipole allowed (EDA)  $P_1(1)$  transition that probes the population in the  $F_1(3/2e)$  level. Two spectra are shown that are taken with the hexapole switched on (red curve) and off (black curve). The MDA and EDA transitions are separated by the  $\Lambda$ -doublet splitting of the ground state of  $0.055 \text{ cm}^{-1}$  and each transition splits due to the hyperfine structure of the  $j = 1/2$  level in the excited  $A^2\Sigma^+$  into two lines separated by  $0.026 \text{ cm}^{-1}$ .

Table S1: Molecular constants of the OH and NO radical.

|               |                      | OH       | NO       |
|---------------|----------------------|----------|----------|
| $B_0$         | ( $\text{cm}^{-1}$ ) | 18.5487  | 1.69611  |
| $A$           | ( $\text{cm}^{-1}$ ) | -139.21  | 123.1393 |
| $p$           | ( $\text{cm}^{-1}$ ) | 0.235    | 0.01172  |
| $q$           | ( $\text{cm}^{-1}$ ) | -0.0391  | 0.00067  |
| $Q_{1,0}$     | ( $ea_0$ )           | 0.6472   | 0.07195  |
| $Q_{2,0}$     | ( $ea_0^2$ )         | 1.2709   | -0.8257  |
| $Q_{2,\pm 2}$ | ( $ea_0^2$ )         | -1.1589  | 1.0158   |
| $Q_{3,0}$     | ( $ea_0^3$ )         | 2.3023   | 0.8946   |
| $Q_{3,\pm 2}$ | ( $ea_0^3$ )         | -0.02894 | -1.4067  |
| $\alpha_0$    | ( $a_0^3$ )          | 7.4774   | 11.5180  |

$\hat{H}_{\text{OH}}$  and  $\hat{H}_{\text{NO}}$  were taken from Eqs. (2) and (6) in Ref. (34) with the rotational constants  $B_0$ , spin-orbit coupling constants  $A$ , and  $\Lambda$ -doubling constants  $p, q$  given in Table S1.

We constructed model interaction potentials which contain the first order electrostatic interactions between the dipole, quadrupole, and octupole moments of OH and NO ( $V_{\text{el}}$ ), and the leading isotropic contributions of the dispersion ( $V_{\text{disp}}$ ) and induction ( $V_{\text{ind}}$ ) interactions. To prevent collapse of the OH-NO complex at short distance, an isotropic short range repulsion term ( $V_{\text{rep}}$ ) was included.

The first order electrostatic interaction was written in the multipole expansion as

$$\hat{V}_{\text{el}} = \sum_{l_A, m_A, m'_A, l_B, m_B, m'_B} \frac{C_{l_A+l_B, m_A+m_B}(\theta_R, \phi_R)^*}{R^{l_A+l_B+1}} (-1)^{l_B} \left[ \frac{(2l_A + 2l_B)!}{(2l_A)!(2l_B)!} \right]^{\frac{1}{2}} \hat{Q}_{l_A m_A}^{(l_A)} D_{m'_A, m_A}^{(l_A)}(\phi_A, \theta_A, 0)^* \hat{Q}_{l_B m_B}^{(l_B)} D_{m'_B, m_B}^{(l_B)}(\phi_B, \theta_B, 0)^* \langle l_A m_A l_B m_B | l_A + l_B, m_A + m_B \rangle, \quad (2)$$

where  $\hat{Q}_{l_X, m_X}$  are the spherical multipole operators (35) for monomers  $X = A$  and  $B$  (OH and NO). The angles  $(\theta_R, \phi_R)$ ,  $(\theta_A, \phi_A)$ , and  $(\theta_B, \phi_B)$  are the spherical polar angles of the vector  $\mathbf{R}$  connecting the centers of mass of the molecules and of the molecular axes of monomers  $A$  and  $B$ , respectively. The symbol  $\langle \dots | \dots \rangle$  denotes a Clebsch-Gordan coefficient,  $C_{l, m}(\theta_R, \phi_R)$  are Racah normalized spherical harmonics, and  $D_{m'_X, m_X}^{(l_X)}(\phi_X, \theta_X, 0)^*$  are Wigner  $D$ -matrix elements. Evaluation of the first order electrostatic interaction requires the multipole moments  $Q_{l_X m_X}$ , which are defined as the diagonal ( $m_X = 0$ ) and off-diagonal ( $m_X = \pm 2$ ) matrix elements of the multipole operators,

$$Q_{l_X m_X} = \langle S_X, \Lambda_X + m_X, \Omega_X + m_X | \hat{Q}_{l_X, m_X} | S_X, \Lambda_X, \Omega_X \rangle, \quad (3)$$

where  $|S_X, \Lambda_X, \Omega_X\rangle$  are the parity unadapted  ${}^2\Pi_\Omega$  electronic wave functions in which  $S_X = 1/2$ ,  $\Lambda_X = \pm 1$ ,  $\Sigma_X = \pm 1/2$ , and  $\Omega_X = \Lambda_X + \Sigma_X$  are the usual Hund's case (a) quantum numbers.

We took into account the multipole moments listed in Table S1, which were calculated at the internally contracted multi-reference configuration interaction (MRCI) with single and double excitations level of theory (36), using the augmented correlation-consistent polarized valence quadruple zeta (aug-cc-pVQZ) basis set (37) with the MOLPRO program package (38). The bond lengths were fixed at  $r_0 = 0.9790 \text{ \AA}$  for OH (39) and  $r_0 = 1.1538 \text{ \AA}$  for NO (40). Matrix elements of  $\hat{V}_{\text{el}}$  in the electronic direct product basis  $|\Lambda_A = \pm 1, \Lambda_B = \pm 1\rangle$  give rise to a  $4 \times 4$  matrix of diabatic potentials. The  $m_X = \pm 2$  components of the multipole operators occurring in the off-diagonal elements of this matrix couple the  $\Omega = 3/2$  and  $1/2$  states, and drive the inelastic transitions between the  $F_1$  and  $F_2$  monomer fine structure states. The anisotropy of  $V_{\text{el}}$ , i.e., its dependence on the orientation of the molecules [Eq. (2)], couples different rotational states of the monomers. The terms with odd  $l_A$  ( $l_B$ ) also contribute to the transitions that change the parity of the states on  $A$  ( $B$ ).

The leading isotropic contributions of the dispersion and induction interactions were calculated from

$$\hat{V}_{\text{disp}} + \hat{V}_{\text{ind}} = -\frac{C_{6,\text{disp}} + C_{6,\text{ind}}}{R^6}. \quad (4)$$

The dispersion coefficient  $C_{6,\text{disp}}$  was computed from the pseudospectral dipole oscillator strength distributions (DOSDs) of NO (41, Table I) and OH (42) as

$$C_{6,\text{disp}} = \frac{3}{2} \sum_{i,j} \frac{f_i^A f_j^B}{\epsilon_i^A + \epsilon_j^B} = 45.2 E_h a_0^6, \quad (5)$$

where  $\epsilon_i^X$  and  $f_i^X$  are the pseudostate excitation energies and oscillator strengths, respectively. For OH the DOSDs were obtained as the average of the  $xx$ ,  $yy$ , and  $zz$  components as given in table II of (42). In that table, these three components are labeled by  $(l, m, l', m', p) = (1, 1, 1, 1, +)$ ,  $(1, 1, 1, 1, -)$ , and  $(1, 0, 1, 0, +)$ , respectively. The induction coefficient was calculated from

$$C_{6,\text{ind}} = (\mu_A)^2 \alpha_0^{(B)} + (\mu_B)^2 \alpha_0^{(A)} = 4.91 E_h a_0^6, \quad (6)$$

with dipole moments  $\mu_X = Q_{1,0}^X$  and static dipole-dipole polarizabilities  $\alpha_x^{(X)}$  from Table S1.

In order to prevent collapse of the OH-NO dimer at short distance we added an isotropic short-range repulsion term

$$V_{\text{rep}} = e^{-\beta(R-R_0)}, \quad (7)$$

with  $\beta = 2 a_0^{-1}$  and  $R_0 = 1.5 a_0$ . We damped the long-range interactions with Tang-Toennies damping functions (43) with the same exponent  $\beta$  as used in the repulsive term.

Although the calculation of the full matrix of diabatic PESs at short range is beyond the capabilities of current theoretical methods, we have performed exploratory *ab initio* calculations for a set of given orientation angles  $\theta_A$ ,  $\theta_B$ , and  $\phi = \phi_B - \phi_A$ . Since the monomers  $A$  and  $B$  have (spin doublet) ground states with spin quantum numbers  $S_A = 1/2$  and  $S_B = 1/2$ , the states of the OH-NO complex can have spin  $S = 0$  (singlet) and 1 (triplet); we computed the interaction energies for each spin  $S$ . The method employed was the complete active space self-consistent field (CASSCF) method with a triple zeta (cc-pVTZ) basis; this method, in contrast

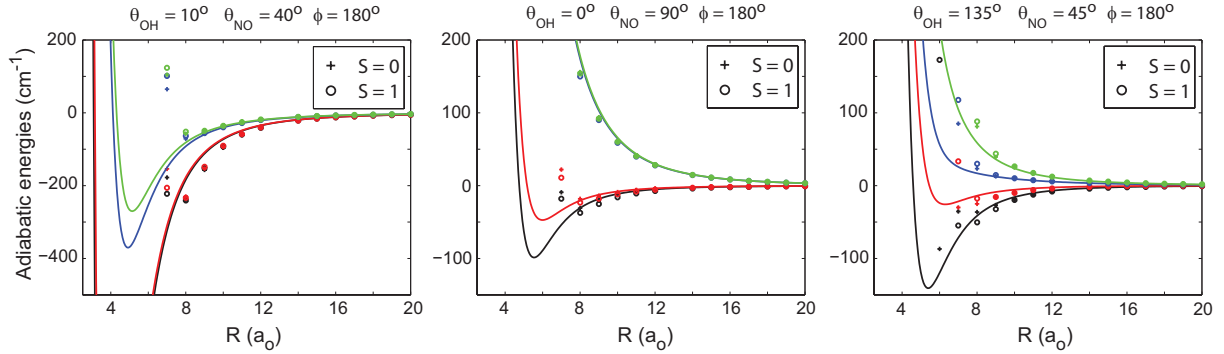


Figure S2: Adiabatic interaction energies for given orientation angles from the model potential (solid curves) and from *ab initio* calculations on the OH-NO complex for spin  $S = 0$  and 1 (data points). Curves and points with the colors black, red, blue and green refer to states of increasing energy order.

with the MRCI method, is size-consistent. *Ab initio* calculations are performed at fixed values of the nuclear coordinates and provide adiabatic potentials. The latter can be compared with the four adiabatic potentials obtained from our model by diagonalization of the  $4 \times 4$  matrix of diabatic potentials defined in this model. Since the CASSCF method used for the direct *ab initio* calculations of the interaction energies is less accurate than the MRCI method used for the calculation of the monomer multipole moments and the basis was smaller, the multipole moments were also calculated with the CASSCF method in the smaller basis. The calculated adiabatic interaction energies for the four lowest states with  $S = 0$  and 1 are shown in Figure S2 and compared to the four adiabatic potentials obtained from our long-range model with the multipole moments computed at the same level of theory.

It is clear from these pictures that the model provides rather accurate interaction energies for distances  $R$  larger than 8-12  $a_0$ . They start to deviate from the *ab initio* data when the OH and NO electronic wave functions overlap; the value of  $R$  where this happens depends on the orientations of the monomers. Also the exchange interactions that split the singlet and triplet energies are determined by the overlap. These exchange interactions depend exponentially on the distance  $R$  and are strongly anisotropic; for some orientations the lower singlet states correspond to a strongly bound HONO species stabilized by covalent bonding, while the triplet states are repulsive or just show a shallow minimum originating from weak noncovalent interactions. Obviously, our model that focuses on the long range interaction energies cannot describe these short-range features.

### Coupled channels calculations

For the Hamiltonian  $\hat{H}$  in Eq. (1) we set up the coupled channels (CC) equations with inelastic scattering boundary conditions, which we solved with the renormalized Numerov method (44, 45). In the channel basis we included all molecular states that are coupled through  $\hat{H}$  in first

order with the initial state [OH  $F_1(3/2f)$ -NO  $F_1(1/2f)$ ]. Hence, we included all (18) OH states with  $j \leq 9/2$  and all (14) NO states with  $j \leq 7/2$ . We employed a space-fixed, parity adapted, total angular momentum ( $J_{\text{tot}}$ ) representation channel basis. For the renormalized Numerov propagation we used an equally spaced grid from 3 to 35  $a_0$  in steps of 0.08  $a_0$ . We solved the CC equations for both parities for 30 partial waves with  $0 \leq J_{\text{tot}} \leq 225$ . The number of coupled channels is 4408, or less for partial waves with small  $J_{\text{tot}}$ . The contributions from other partial waves to the inelastic cross sections were found by cubic spline interpolation. To test the correctness of the scattering code, two versions were written independently by two of the authors, one in Scilab and one in Fortran and Matlab. We verified that the results are converged with respect to the grid range, step size,  $J_{\text{tot}}$ , as well as the number of partial waves that were explicitly included.

### Sensitivity of the results with respect to changes in the model Hamiltonian

We repeated the calculation with a model Hamiltonian in which we set the octupole moments of OH and NO to zero and in which we eliminated the basis functions with OH( $j = 9/2$ ) or NO( $j = 7/2$ ), i.e., again keeping the states that are coupled in first order. As a result, the cross sections for the OH  $F_1(3/2e)$  product state were reduced by only about 4 %. The cross sections for the OH  $F_1(5/2e)$ ,  $F_2(1/2e)$ , and  $F_1(7/2e)$ , channels were reduced by about 12 %, 22 %, and 55 %, respectively. Next, we took the original model Hamiltonian and channel basis, but increased the isotropic repulsion by increasing  $R_0$  by 1  $a_0$  (i.e., we set  $R_0 = 2.5 a_0$  in Eq. 7). Again, the parity changing  $F_1(3/2e)$  cross sections are hardly affected: they change by less than 4 %. This more repulsive potential resulted in smaller cross sections for the OH  $F_1(5/2e)$ ,  $F_2(1/2e)$ , and  $F_1(7/2e)$  channels, by about 25 %, 20 %, and 74 %, respectively. Dropping the isotropic dispersion and inductions terms in the Hamiltonian also had little effect on the parity changing channel, but it reduced the cross sections for the other channels. We did not attempt to model the exchange interaction. This interaction is short-ranged, anisotropic, and decays exponentially with the intermolecular distance. It also lifts the degeneracy between singlet and triplet potentials, and hence it can be expected to affect fine-structure changing cross sections.

From these observations, we concluded that the  $F_1(3/2e)$  channel is dominated by the long-range electrostatic interaction, whereas the rotationally and spin-orbit inelastic collisions are also sensitive to the short-range interaction. The sizable contribution of the octupole moments to the scattering cross sections implies that higher-order anisotropic terms in the Hamiltonian may be required to improve the agreement with the experimentally determined cross sections.

## 3 Data analysis

### Density-to-flux transformation

The measured scattering signals do in general not directly relate to cross sections. In crossed beam experiments, the scattering signal  $S_j(T)$  that is recorded at time  $T$  relates directly to the

number of particles  $N_j$  that have been scattered into quantum state  $j$ , and that are within the probe laser volume  $V_{probe}$  at time  $T$  (46, 47):

$$S_j(T) \propto P_j(T) N_j(T), \quad (8)$$

where the factor  $P_j(T)$  represents the probability for the scattered particles to be detected at time  $T$ . The number of scattered particles follows from the beam geometries and the scattering cross section:

$$N_j(T) = \int \int n_{OH}(\vec{r}, t) n_{NO}(\vec{r}, t) \sigma_j g dV_{int} dt, \quad (9)$$

where  $n_{OH}(\vec{r}, t)$  and  $n_{NO}(\vec{r}, t)$  are the density distributions of the parent OH and NO radical beams, respectively,  $\sigma_j$  is the scattering cross section to populate state  $j$ , and  $g$  is the magnitude of the relative velocity vector of the colliding particles. We assumed that for a given collision energy  $E$ , there is a single value of  $g$  that describes the relative velocity of the colliding beams. The integral must be performed over the beam intersection volume  $V_{int}$ , and over all times  $t$  until the probe laser fires.

In general, the evaluation of the detection probability  $P_j(T)$  requires knowledge over the post-collision velocity vector of the scattered particles, and hence information on the differential cross section. Below, we show that for our experimental conditions, the detection probability  $P_j(T)$  was unity for all collision energies, and for all final states  $j$  that were probed, greatly simplifying the analysis.

In its propagation direction, the Stark-decelerated packet of OH radicals was small compared to the NO radical beam, and the temporal overlap between the two beams was exclusively defined by the Stark-decelerated OH radicals. This is illustrated in Figure S3, in which the measured normalized arrival time distributions of the NO and OH radical packets are shown. The distribution for the OH radical pertains to the situation where the Stark decelerator was programmed to produce a packet of OH radicals with a mean velocity of 625 m/s ( $E = 220 \text{ cm}^{-1}$ ). In this case, a packet of OH radicals was created with the largest possible extent in the propagation direction. Even in this case, the arrival time distribution of the OH radicals had a width (FWHM) of only 25  $\mu\text{s}$ . It is seen that the intensity of the NO radical beam was approximately constant during the overlap with the packet of OH radicals.

To model the density distribution of the NO radical beam, we therefore assumed no temporal dependence, and no change of the spatial distribution along the propagation direction. We defined a right-handed coordinate system, and set the origin of this coordinate system at the crossing point of the centerlines of both molecular beams. We defined the  $x$ -axis and the  $y$ -axis as the OH and NO propagation directions, respectively. In the radial direction, the density distribution could best be described by Gaussian profiles:

$$n_{NO}(\vec{r}, t) = n_{NO}(\vec{r}) = n_{max}^{NO} e^{-\alpha(x^2+z^2)}, \quad (10)$$

where  $n_{max}^{NO}$  represents the maximum density of the NO radical beam. The parameter  $\alpha = 4 \ln 2 / (d_{NO})^2$  was estimated from numerical trajectory simulations of the NO radical beam that

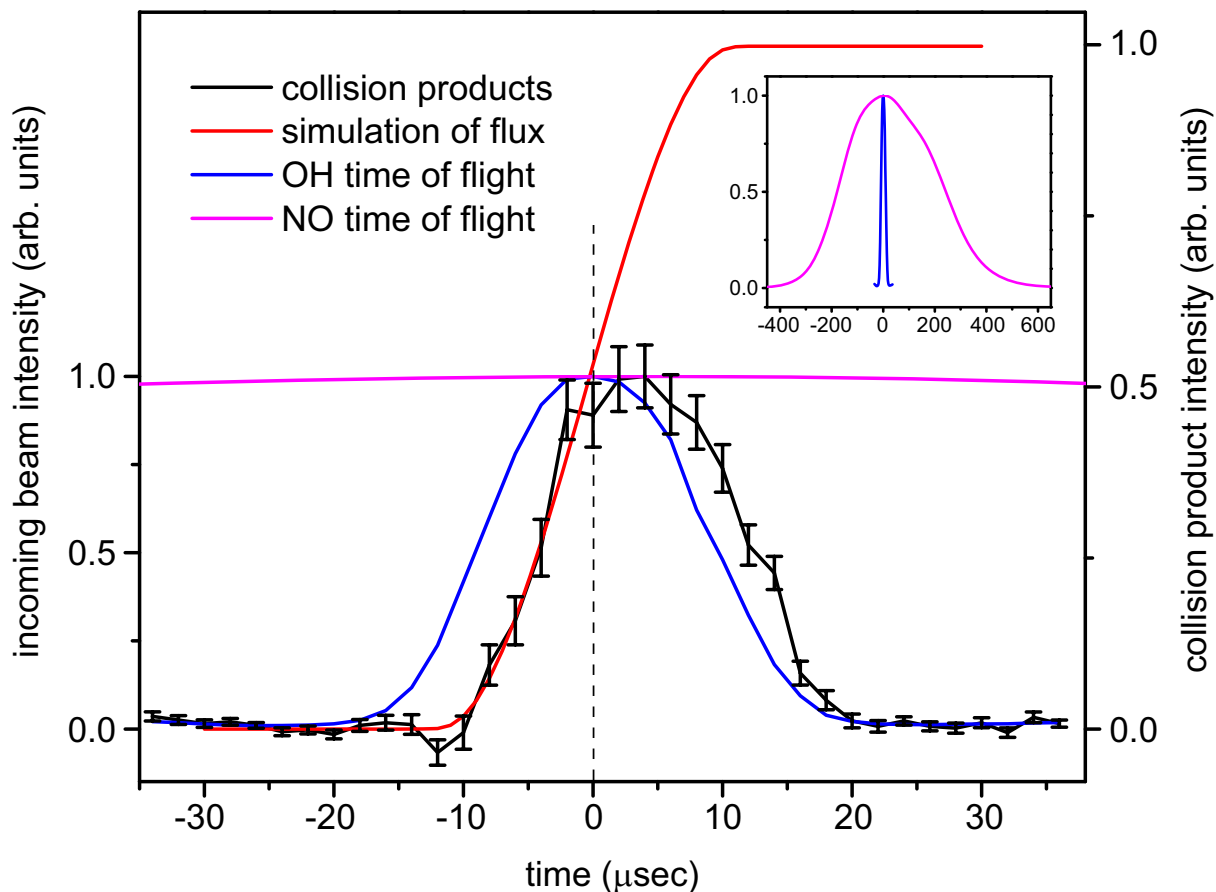


Figure S3: Comparison of the temporal dependence of the scattering signal  $S_j(T)$  (black), the result of Eq. 8 (red), the OH radical beam (blue) and the NO radical beam (violet). The y-axis on the left side relates to the two radical beams, and the y-axis on the right side relates to the scattering signal and the simulation. All curves are scaled to one to facilitate a comparison of the temporal profiles. Vertical error bars indicate combined estimates of both statistical and systematic errors ( $2\sigma$ ) from  $> 50,000$  shots of the experiment. The inset shows an enlarged time range to visualize the broad temporal distribution of the NO radical in relation to the temporal width of the OH radical beam. Note that the temporal distribution of the scattering signal is shifted to later times with respect to the arrival time distribution of the reagent packet of OH radicals. This is the result of the difference between the beam intersection volume  $V_{int}$  and the probe laser volume  $V_{probe}$ , with  $V_{probe} > V_{int}$ . The vertical dashed line, at  $T = 0$ , corresponds to the time at which the laser is fired when cross sections are measured.

propagates through the electrostatic hexapole, and from the measured two-dimensional images of the NO beam. The NO beam was best characterized using  $d_{NO} = 1.2$  mm (FWHM). The packet of OH radicals traveled along the  $x$ -axis with a velocity  $v_{OH}$ . The spatial distribution of the packet of OH radicals was accurately known from numerical trajectory simulations of the deceleration process. In the transverse direction, the spatial distribution could be accurately described by a Gaussian distribution. In the propagation direction, however, the distribution was best described by a parabolic distribution:

$$n_{OH}(\vec{r}, t) = n_{max}^{OH} (1 - b(x - v_{OH}t)^2) e^{-\beta(y^2 + z^2)}, \quad (11)$$

where  $n_{max}^{OH}$  represents the maximum density of the OH radical beam. Outside of the intersection points  $v_{OH}t \pm \sqrt{\frac{1}{b}}$  with the  $x$ -axis this function was defined to be 0. The parameters  $n_{max}^{OH}$ ,  $b$ , and  $\beta = 4 \ln 2 / (d_{OH})^2$  depend on the settings of the Stark decelerator, and were thus different for every value of  $v_{OH}$  that was produced. The parameters  $b$  and  $d_{OH}$  (FWHM) were fitted from the spatial distributions that resulted from three dimensional trajectory simulations of the deceleration process, and are given in Table S2.

By evaluating the integrals in Eq. 8 assuming  $P_j(T) = 1$ , the temporal dependence of the scattering signal  $S_j(T)$  as shown in Figure S3 was obtained for a collision energy of  $220 \text{ cm}^{-1}$  ( $v_{OH} = 625$  m/s). This curve was calculated for the  $F_1(3/2e)$  scattering channel, i.e., for the situation in which the scattered OH radicals had the largest recoil velocity vector. The temporal dependence of the experimentally observed scattering signal is shown superimposed to the simulated curve. Up to time  $T = 0$ , the time at which the two beams were at the maximum of their overlap and the probe laser was fired (indicated with the vertical dashed line in Figure S3), we observed that the measured collision signal  $S_j(T)$  closely followed the simulated curve. At later times, the scattered OH radicals had moved out of the probe laser volume, and the scattering signal was reduced. We thus concluded that under our experimental conditions, at the time when the probe laser fired, all scattered OH radicals were within the detection laser volume, and were detected with equal probability. A similar analysis had been made at collision energies of  $80 \text{ cm}^{-1}$ ,  $160 \text{ cm}^{-1}$ , and  $240 \text{ cm}^{-1}$  (data not shown), leading to identical conclusions. In our experiments, the laser induced fluorescence detector thus acted as a flux detector, and a density-to-flux transformation was not required to convert measured scattering signals into cross sections. This favorable situation resulted from the small dimensions of the Stark-decelerated packets of OH radicals, and the large probe laser volume that was possible using laser induced fluorescence detection.

### Determination of relative cross sections and excitation functions

For a given scattering channel, the collision energy dependence of the state-to-state cross section (referred to as the excitation function) was determined by evaluating the integrals of Eq. 9 for every collision energy  $E$ :

$$\sigma_j(E) \propto \frac{S_j(E, T)}{g(E) f(E, T)}, \quad (12)$$

Table S2: Simulation parameters for all collision energies and the two carrier gases Argon and Krypton that were used to generate the OH molecular beam. Column one shows all collision energies that have been used to measure the collision signals and column two shows the corresponding velocities of the OH beam produced by the Stark decelerator. The parameters  $b$  and  $d_{OH}$  are estimated from numerical trajectory simulation of the decelerator.  $S_{OH}$  represents the measured peak signal intensity of the reagent packets of OH radicals.

| <b>argon</b>                  |                   |                            |                  |                    |                          |
|-------------------------------|-------------------|----------------------------|------------------|--------------------|--------------------------|
| $E_c$<br>( $\text{cm}^{-1}$ ) | $v_{OH}$<br>(m/s) | $b$<br>( $\text{m}^{-2}$ ) | $d_{OH}$<br>(mm) | $S_{OH}$<br>(a.u.) | $n_{max}^{OH}$<br>(a.u.) |
| 300                           | 752               | 7.0                        | 0.86             | 0.34               | 0.50                     |
| 280                           | 722               | 5.1                        | 0.85             | 0.51               | 0.67                     |
| 260                           | 691               | 3.5                        | 0.85             | 0.70               | 0.75                     |
| 240                           | 659               | 2.8                        | 0.82             | 0.88               | 0.91                     |
| 220                           | 625               | 2.1                        | 0.79             | 1.00               | 1.00                     |
| 210                           | 606               | 2.4                        | 0.82             | 0.96               | 0.94                     |
| 200                           | 588               | 2.8                        | 0.82             | 0.88               | 0.90                     |
| 190                           | 569               | 3.1                        | 0.86             | 0.75               | 0.74                     |
| 180                           | 549               | 3.7                        | 0.90             | 0.70               | 0.69                     |
| 160                           | 507               | 4.7                        | 0.90             | 0.52               | 0.58                     |
| 140                           | 461               | 7.5                        | 0.90             | 0.32               | 0.46                     |
| <b>krypton</b>                |                   |                            |                  |                    |                          |
| $E_c$<br>( $\text{cm}^{-1}$ ) | $v_{OH}$<br>(m/s) | $b$<br>( $\text{m}^{-2}$ ) | $d_{OH}$<br>(mm) | $S_{OH}$<br>(a.u.) | $n_{max}^{OH}$<br>(a.u.) |
| 160                           | 507               | 2.2                        | 0.91             | 0.82               | 0.63                     |
| 140                           | 461               | 2.5                        | 0.84             | 0.73               | 0.69                     |
| 130                           | 437               | 2.8                        | 0.91             | 0.65               | 0.55                     |
| 120                           | 411               | 3.0                        | 0.99             | 0.53               | 0.39                     |
| 110                           | 383               | 3.5                        | 0.96             | 0.49               | 0.41                     |
| 100                           | 353               | 4.0                        | 1.13             | 0.39               | 0.25                     |
| 90                            | 320               | 4.5                        | 1.18             | 0.33               | 0.20                     |
| 80                            | 283               | 5.4                        | 1.26             | 0.24               | 0.15                     |
| 70                            | 242               | 5.5                        | 1.39             | 0.18               | 0.91                     |

where the variable  $E$  was added to indicate the parameters that depend on the collision energy. The beam overlap factor  $f(E)$  is given by

$$f(E, T) = \int \int_{-\infty}^T n_{OH}(E, \vec{r}, t) n_{NO}(\vec{r}, t) dV_{int} dt \quad (13)$$

and was evaluated Eq. 10 and 11 and the parameters given in Table S2.

The relative peak densities  $n_{max}^{OH}(E)$  were determined from the measured relative peak signal intensities  $S_{OH}(E)$  of the OH packets, that are proportional to the total number  $N_{OH}(E)$  of reagent OH radicals that were within the probe laser volume:  $S_{OH}(E) \propto N_{OH}(E)$  with

$$N_{OH}(E) = n_{max}^{OH}(E) \int (1 - bx^2) e^{-\beta(y^2+z^2)} dV_{probe}. \quad (14)$$

If we set  $n_{max}^{OH}(E = 220 \text{ cm}^{-1}) = 1$ , the values for  $n_{max}^{OH}(E)$  as given in Table 1 were obtained.

To relate the excitation functions with respect to each other, the relative state-to-state cross sections were evaluated at a single collision energy  $E = 220 \text{ cm}^{-1}$  via additional measurements of the ratios between the collision signals  $S_j$ . The determination of these ratios, however, was complicated by the necessary use of two different laser systems to detect the collision induced population into the four levels. The  $F_1(5/2e)$ ,  $F_1(7/2e)$ , and the  $F_2(j = 1/2e)$  levels were probed using a pulsed dye laser, whereas the  $F_1(3/2e)$  channel could only be probed using a pulsed dye amplified ring dye laser system.

The pulsed dye laser had a bandwidth that is sufficiently large to cover the Doppler shifts in the spectral profiles due to the recoil velocities of the scattered particles. Care was taken to excite the optical transitions under saturated conditions. Under these conditions, fluorescence signal intensities can be related to collision induced populations taking the excitation rates (ER) into account that apply to saturated laser induced fluorescence detection. The ER rates that apply to our experimental conditions are given in ref. (13), and were used to determine the relative cross sections for the  $F_1(5/2e)$ ,  $F_1(7/2e)$ , and the  $F_2(1/2e)$  channels.

The pulsed dye amplified ring dye laser system had a bandwidth that is much narrower than the Doppler profile of the scattering products. In addition, in order to effectively separate the MDA transitions that probe the initial  $F_1(3/2f)$  level from the EDA transitions that probe the  $F_1(3/2e)$  level, the transitions were induced under unsaturated conditions. Hence, the  $F_1(3/2e)$  channel was probed by scanning the laser over an energy range that covered both the MDA and EDA transitions. The collision induced population was determined by evaluating the integrated intensity difference of the spectra recorded with the voltages on the hexapole that focuses the NO radical beam switched on and off, respectively.

To relate the  $F_1(3/2e)$  channel to the other three channels, the relative state-to-state cross sections for the  $F_1(3/2e)$  and the  $F_1(5/2e)$  channels was determined separately. For this, the collision induced population in the  $F_1(5/2e)$  channel was also measured using the pulsed dye amplified ring dye laser system. The ratio in fluorescence signal intensities was converted into relative cross sections taking the appropriate absorption coefficients of the transitions into account. Together, the measured ratios yielded the relative cross sections for all four levels.

### Determination of absolute cross sections

In addition to the relative cross sections, we have determined the *absolute* cross section for the  $F_1(3/2e)$  channel at a collision energy of  $E = 220 \text{ cm}^{-1}$ . The cross section  $\sigma_j$  for a given scattering channel  $j$  is given by (see Eq. 9 and 13):

$$\sigma_j = \frac{N_j}{gf(T)}. \quad (15)$$

In general, the largest difficulty in evaluating the *absolute* numbers for  $N_j$  and  $f(T)$  is to find the appropriate relation between number of photons detected in the laser induced fluorescence detection scheme, and the corresponding number of molecules that are in the probe laser volume.

We factored out the peak densities  $n_{max}^{OH}$  and  $n_{max}^{NO}$  of the reagent beams from the beam overlap function  $f(T)$ :

$$f'(T) = \frac{1}{n_{max}^{OH} n_{max}^{NO}} f(T), \quad (16)$$

and introduced the function  $h$  that describes the volume overlap between the OH reagent beam and the probe laser beam:

$$h = \int (1 - bx^2) e^{-\beta(y^2+z^2)} dV_{probe} \quad (17)$$

such that

$$n_{max}^{OH} = \frac{N_{OH}}{h}. \quad (18)$$

Eq. 15, 16, and 18 can then be combined to

$$\sigma_j = \frac{N_j}{N_{OH}} \frac{h}{g} \frac{1}{f'(T) n_{max}^{NO}}. \quad (19)$$

The factor  $h/g f'(T)$  could easily be evaluated from Eq. 10 and 11, and from the parameters of Table S2.

The cross section was evaluated from a measurement of the NO beam density and a measurement of the ratio  $N_j/N_{OH}$ . It is noted that although the scattering of two state-selected molecules is experimentally significantly more complex and difficult than the scattering of state-selected molecules with rare gas atoms, the ability to probe the collision partner with laser-based detection techniques represents a formidable advantage, and allows for the accurate measurement of beam densities. The peak density  $n_{max}^{NO}$  of the NO reagent beam was determined from a calibrated measurement of the number  $N_{NO}$  of NO radicals in the probe laser volume. The number of photons  $N_{photons}$  that was detected depends on the number of NO radicals  $N_{NO}$  via

$$N_{NO} = \frac{N_{photons}}{\Omega T Q \epsilon}, \quad (20)$$

where  $\Omega$  and  $T$  are the solid angle and transmission efficiency of the light collection system, respectively,  $Q$  is the quantum efficiency of the light detector, and  $\epsilon$  represents the fraction of the molecules that contributed to the fluorescence signal upon laser excitation. Using a calibrated spectrometer, a value for  $T$  of  $0.87 \pm 0.05$  was measured. The quantum efficiency of the photomultiplier tube (PMT) was specified by the supplier as  $0.3 \pm 0.03$ . Optical excitation of the NO radicals was performed under completely saturated conditions, such that  $\epsilon = 0.5$ . No light collection lens was used in these measurements such that  $\Omega$  was exclusively determined by the distance  $r$  of the PMT with respect to the probe volume, and the active area of the PMT which was reduced by a pinhole with 1.0 mm diameter. We have counted  $N_{photons}$  for four different values of  $r$ , ranging from 1.5 m to 2.1 m, and the expected linear dependency of  $N_{photons}$  on  $\Omega$  was observed. For the largest solid angle used, we observed on average 3.9 photons per shot, resulting in  $N_{NO} = (1.0 \pm 0.3) \times 10^9$  molecules. Using the spatial distribution of the NO packet as defined in Eq. 10 and the probe laser volume  $V_{probe}$ , we determined the peak density  $n_{max}^{NO} = (9 \pm 3) \times 10^{10}$  molecules  $\text{cm}^{-3}$ .

The ratio  $N_j/N_{OH}$  can directly be inferred from the ratio of the detector signals that were recorded when the reagent and product OH radicals are probed. Under our experimental conditions, however, the number of product OH radicals  $N_j(E)$  was orders of magnitude lower than the number of reagent OH radicals  $N_{OH}(E)$ , rendering such measurement difficult. We have used the magnetic dipole allowed (MDA)  $P_1(1)'$  transition to probe  $N_{OH}$ , and the electric dipole allowed (EDA)  $P_1(1)'$  transition to probe  $N_j$ . The advantage of this approach was that we obtained information on both  $N_{OH}$  and  $N_j$  in a single spectral scan of the narrowband dye laser. Both transitions were induced under unsaturated conditions, such that the signal levels that probe  $N_{OH}$  and  $N_j$  could be measured using identical detector settings.

The value for  $N_j/N_{OH}$  was then established from the measured signal ratio and the factor  $k$  that represents the ratio of transition strengths of the EDA  $P_1(1)$  and the MDA  $P_1(1)'$  transitions. The value for  $k$  was determined from theoretical calculations (48). In these calculations, the population distribution of the OH radicals over the  $F = 2$  and  $F = 1$  hyperfine levels of the  $F_1(3/2f)$  and  $F_1(3/2e)$  states was taken into account. This population distribution of the reagent packet of OH  $F_1(3/2f)$  radicals followed from the measured hyperfine state dependent transmission efficiency of the Stark decelerator; a population of 77 % in the  $F = 2$  and 23 % in  $F = 1$  level was measured with equal populations in the different  $M_F$  states. No polarization effects of the laser and no specific magnetic field direction were taken into account. We assumed that collisions populating the  $F_1(3/2e)$  level were dominated by the  $\Delta F = \Delta j = 0$  propensity rule, such that the hyperfine states were conserved during the collision (49). In addition, any collision-induced polarization would be largely destroyed by nuclear hyperfine depolarization. Under these conditions, we found  $k = 2576$ . It is noted that the uncertainty in the value for  $k$  was primarily due to uncertainties in the theoretically calculated transition strengths, and the exact experimental conditions such as laser polarization, external magnetic fields, and distribution over the various hyperfine states. These experimental factors can in principle be precisely controlled (48), although in the present experiments an exquisite level of control was not available. We therefore estimated the accuracy of the value for  $k$  to about

20 %. Our measurements of  $n_{max}^{NO}$  in combination with the measured ratio between reagent and product number of molecules  $N_j/N_{OH}$  were combined to yield a total inelastic scattering cross section for the  $F_1(3/2e)$  channel at a collision energy of  $220 \text{ cm}^{-1}$  of  $90 \pm 38 \text{ \AA}^2$ .

## References

1. R. D. Levine, R. B. Bernstein, *Molecular reaction dynamics and chemical reactivity* (Oxford University Press, New York, 1987).
2. D. W. Chandler, S. Stolte, Chapter 5 in *Tutorials in Molecular Reaction Dynamics*, Ed. M. Brouard and C. Vallance, (Royal Society of Chemistry, 2010).
3. S. Weinreb, A. H. Barrett, M. L. Meeks, J. C. Henry, *Nature* **200**, 829 (1963).
4. A. Schiffman, D. W. Chandler, *Int. Rev. Phys. Chem.* **14**, 371 (1995).
5. S. Stolte, *Nature* **353**, 391 (1991).
6. D. Watanabe, H. Ohoyama, T. Matsumura, T. Kasai, *Phys. Rev. Lett.* **99**, 043201 (2007).
7. K. T. Lorenz, *et al.*, *Science* **293**, 2063 (2001).
8. C. J. Eyles, *et al.*, *Nature Chemistry* **3**, 597 (2011).
9. H. Kohguchi, T. Suzuki, M. H. Alexander, *Science* **294**, 832 (2001).
10. S. Y. T. van de Meerakker, H. L. Bethlem, G. Meijer, *Nature Physics* **4**, 595 (2008).
11. S. Y. T. van de Meerakker, H. L. Bethlem, N. Vanhaecke, G. Meijer, *Chemical Reviews* **112**, 4828 (2012).
12. J. J. Gilijamse, S. Hoekstra, S. Y. T. van de Meerakker, G. C. Groenenboom, G. Meijer, *Science* **313**, 1617 (2006).
13. L. Scharfenberg, *et al.*, *Phys. Chem. Chem. Phys.* **12**, 10660 (2010).
14. P. Hartogh, *et al.*, *Nature* **478**, 218 (2011).
15. G. Paterson, M. L. Costen, K. G. McKendrick, *Int. Rev. Phys. Chem.* **31**, 69 (2012).
16. D. C. Clary, *Ann. Rev. Phys. Chem.* **41**, 61 (1990).
17. I. W. M. Smith, *Annu. Rev. Astron. Astrophys.* **49**, 29 (2011).
18. R. B. Bernstein, *Science* **144**, 141 (1964).

19. B. C. Sawyer, *et al.*, *Phys. Chem. Chem. Phys.* **13**, 19059 (2011).
20. C. Berteloite, *et al.*, *Phys. Rev. Lett.* **105**, 203201 (2010).
21. K. Schreel, J. J. ter Meulen, *J. Chem. Phys.* **105**, 4522 (1996).
22. The labels  $X^2\Pi_{3/2}$ ,  $X^2\Pi_{1/2}$ ,  $v$ , and  $j$  indicate the electronic states, the vibrational state and rotational state of both the OH and the NO radical, respectively. The spectroscopic symmetry labels  $e$  and  $f$  refer to the total parity of the electronic wavefunction, exclusive of rotation. The total inversion parity is indicated by the additional labels + and –.
23. H. Kohguchi, T. Suzuki, *Annu. Rep. Prog. Chem., Sect. C* **98**, 421 (2002).
24. M. T. Vonk, J. A. Bacon, C. F. Giese, W. R. Gentry, *J. Chem. Phys.* **106**, 1353 (1997).
25. K. Sharkey, I. R. Sims, I. W. M. Smith, P. Bocherel, B. R. Rowe, *J. Chem. Soc. – Faraday Trans.* **90**, 3609 (1994).
26. Materials and methods are available as supplementary material on *Science Online*.
27. L. Scharfenberg, H. Haak, G. Meijer, S. Y. T. van de Meerakker, *Phys. Rev. A* **79**, 023410 (2009).
28. It was verified that all scattered molecules are detected with equal probability, and no density-to-flux correction was needed to relate the measured scattering signals to relative inelastic cross sections. See supplementary material for more information.
29. L. Scharfenberg, *et al.*, *Eur. Phys. J. D* **65**, 189 (2011).
30. P. J. Dagdigian, M. H. Alexander, *J. Chem. Phys.* **130**, 094303 (2009).
31. M. Nguyen, R. Sumathi, D. Sengupta, J. Peeters, *Chem. Phys.* **230**, 1 (1998).
32. The OH-NO spin states with  $S = 0$  and  $S = 1$  are not distinguished in our model; the  $4 \times 4$  matrices for each spin state are therefore identical.
33. Although the quadrupole moment vanishes in the  $j = 1/2$  state of NO, the quadrupole moment in the molecular frame contributes to the collisions producing NO states with  $j = 3/2$  and  $5/2$  that yield important contributions to the measured cross sections.
34. G. C. Groenenboom, A. V. Fishchuk, A. van der Avoird, *J. Chem. Phys.* **131**, 124307 (2009).
35. A. van der Avoird, P. E. S. Wormer, F. Mulder, R. M. Berns, *Top. Curr. Chem.* **93**, 1 (1980).
36. H.-J. Werner, P. J. Knowles, *J. Chem. Phys.* **89**, 5803 (1988).

37. T. H. Dunning, *J. Chem. Phys.* **90**, 1007 (1989).
38. MOLPRO, a package of *ab initio* programs, H.-J. Werner, P. J. Knowles, R. Lindh, F. R. Manby, M. Schütz, and others, see <http://www.molpro.net>.
39. J. P. Maillard, J. Chauville, A. W. Mantz, *J. Mol. Spectrosc.* **63**, 120 (1976).
40. J. W. C. Johns, J. Reid, D. W. Lepard, *J. Mol. Spectrosc.* **65**, 155 (1977).
41. D. J. Margoliash, W. J. Meath, *J. Chem. Phys.* **68**, 1426 (1978).
42. D. Spelsberg, *J. Chem. Phys.* **111**, 9625 (1999).
43. K. T. Tang, J. P. Toennies, *J. Chem. Phys.* **80**, 3726 (1984).
44. B. R. Johnson, *J. Chem. Phys.* **69**, 4678 (1978).
45. B. R. Johnson, *NRCC Proceedings* **5**, 86 (1979).
46. D. M. Sonnenfroh, K. Liu, *Chem. Phys. Lett.* **176**, 183 (1991).
47. Ch. Naulin, M. Costes, A. Benseddik, G. Dorthé, *Laser Chem.* **8**, 283 (1988).
48. M. Kirste, *et al.* *J. Chem. Phys.* **137**, 101101 (2012).
49. C. D. Ball, F. C. De Lucia, *Chem. Phys. Lett.* **300**, 227 (1999).

## References

1. R. D. Levine, R. B. Bernstein, *Molecular Reaction Dynamics and Chemical Reactivity* (Oxford University Press, New York, 1987).
2. D. W. Chandler, S. Stolte, in *Tutorials in Molecular Reaction Dynamics*, M. Brouard, C. Vallance, Eds. (Royal Society of Chemistry, Cambridge, 2010), chapter 5.
3. S. Weinreb, A. H. Barrett, M. L. Meeks, J. C. Henry, Radio observations of OH in the interstellar medium. *Nature* **200**, 829 (1963). [doi:10.1038/200829a0](https://doi.org/10.1038/200829a0)
4. A. Schiffman, D. W. Chandler, Experimental measurements of state resolved, rotationally inelastic energy transfer. *Int. Rev. Phys. Chem.* **14**, 371 (1995). [doi:10.1080/01442359509353315](https://doi.org/10.1080/01442359509353315)
5. S. Stolte, Aiming the molecular arrow. *Nature* **353**, 391 (1991). [doi:10.1038/353391a0](https://doi.org/10.1038/353391a0)
6. D. Watanabe, H. Ohoyama, T. Matsumura, T. Kasai, Effect of mutual configuration between molecular orientation and atomic orientation in the oriented Ar (3P<sub>2</sub>)+oriented CF<sub>3</sub>H reaction. *Phys. Rev. Lett.* **99**, 043201 (2007). [doi:10.1103/PhysRevLett.99.043201](https://doi.org/10.1103/PhysRevLett.99.043201) [Medline](#)
7. K. T. Lorenz *et al.*, Direct measurement of the preferred sense of NO rotation after collision with argon. *Science* **293**, 2063 (2001). [doi:10.1126/science.1062754](https://doi.org/10.1126/science.1062754) [Medline](#)
8. C. J. Eyles *et al.*, Interference structures in the differential cross-sections for inelastic scattering of NO by Ar. *Nat. Chem.* **3**, 597 (2011). [doi:10.1038/nchem.1071](https://doi.org/10.1038/nchem.1071) [Medline](#)
9. H. Kohguchi, T. Suzuki, M. H. Alexander, Fully state-resolved differential cross sections for the inelastic scattering of the open-shell NO molecule by Ar. *Science* **294**, 832 (2001). [doi:10.1126/science.1063774](https://doi.org/10.1126/science.1063774) [Medline](#)
10. S. Y. T. van de Meerakker, H. L. Bethlem, G. Meijer, Taming molecular beams. *Nat. Phys.* **4**, 595 (2008). [doi:10.1038/nphys1031](https://doi.org/10.1038/nphys1031)
11. S. Y. T. van de Meerakker, H. L. Bethlem, N. Vanhaecke, G. Meijer, Manipulation and control of molecular beams. *Chem. Rev.* **112**, 4828 (2012). [doi:10.1021/cr200349r](https://doi.org/10.1021/cr200349r) [Medline](#)
12. J. J. Gilijamse, S. Hoekstra, S. Y. T. van de Meerakker, G. C. Groenenboom, G. Meijer, Near-threshold inelastic collisions using molecular beams with a tunable velocity. *Science* **313**, 1617 (2006). [doi:10.1126/science.1131867](https://doi.org/10.1126/science.1131867) [Medline](#)
13. L. Scharfenberg *et al.*, State-to-state inelastic scattering of Stark-decelerated OH radicals with Ar atoms. *Phys. Chem. Chem. Phys.* **12**, 10660 (2010). [doi:10.1039/c004422a](https://doi.org/10.1039/c004422a) [Medline](#)
14. P. Hartogh *et al.*, Ocean-like water in the Jupiter-family comet 103P/Hartley 2. *Nature* **478**, 218 (2011). [doi:10.1038/nature10519](https://doi.org/10.1038/nature10519) [Medline](#)
15. G. Paterson, M. L. Costen, K. G. McKendrick, Collisional depolarisation of rotational angular momentum: influence of the potential energy surface on the collision dynamics? *Int. Rev. Phys. Chem.* **31**, 69 (2012). [doi:10.1080/0144235X.2012.659046](https://doi.org/10.1080/0144235X.2012.659046)

16. D. C. Clary, Fast chemical reactions: Theory challenges experiment. *Annu. Rev. Phys. Chem.* **41**, 61 (1990). [doi:10.1146/annurev.pc.41.100190.000425](https://doi.org/10.1146/annurev.pc.41.100190.000425)
17. I. W. M. Smith, Laboratory astrochemistry: Gas-phase processes. *Annu. Rev. Astron. Astrophys.* **49**, 29 (2011). [doi:10.1146/annurev-astro-081710-102533](https://doi.org/10.1146/annurev-astro-081710-102533)
18. R. B. Bernstein, Molecular beam scattering at thermal energies. *Science* **144**, 141 (1964). [doi:10.1126/science.144.3615.141](https://doi.org/10.1126/science.144.3615.141) [Medline](#)
19. B. C. Sawyer *et al.*, Cold heteromolecular dipolar collisions. *Phys. Chem. Chem. Phys.* **13**, 19059 (2011). [doi:10.1039/c1cp21203f](https://doi.org/10.1039/c1cp21203f) [Medline](#)
20. C. Berteloite *et al.*, Kinetics and dynamics of the S(1D2) + H<sub>2</sub> → SH + H reaction at very low temperatures and collision energies. *Phys. Rev. Lett.* **105**, 203201 (2010). [doi:10.1103/PhysRevLett.105.203201](https://doi.org/10.1103/PhysRevLett.105.203201) [Medline](#)
21. K. Schreel, J. J. ter Meulen, Determination of  $\Lambda$ -doublet resolved cross-sections for inelastic scattering of OH by para- and normal-H<sub>2</sub>. *J. Chem. Phys.* **105**, 4522 (1996). [doi:10.1063/1.472328](https://doi.org/10.1063/1.472328)
22. The labels  $X^2\Pi_{3/2}$ ,  $X^2\Pi_{1/2}$ ,  $v$ , and  $j$  indicate the electronic states, the vibrational state, and the rotational state of both the OH and the NO radical, respectively. The spectroscopic symmetry labels  $e$  and  $f$  refer to the total parity of the electronic wave function, exclusive of rotation. The total inversion parity is indicated by the additional labels + and –.
23. H. Kohguchi, T. Suzuki, State-to-state rotational inelastic scattering of free radicals. *Annu. Rep. Prog. Chem. Sect. C* **98**, 421 (2002). [doi:10.1039/B111167C](https://doi.org/10.1039/B111167C)
24. M. T. Vonk, J. A. Bacon, C. F. Giese, W. R. Gentry, Differential cross sections for rotationally inelastic collisions of NO( $2\Pi_{1/2}$ ,  $j \leq 2.5$ ) with NO( $2\Pi_{1/2}$ ,  $j \leq 2.5$ ) at a kinetic energy of 442 cm<sup>-1</sup>. *J. Chem. Phys.* **106**, 1353 (1997). [doi:10.1063/1.473972](https://doi.org/10.1063/1.473972)
25. P. Sharkey, I. R. Sims, I. W. M. Smith, P. Bocherel, B. R. Rowe, Pressure and temperature dependence of the rate constants for the association reaction of OH radicals with NO between 301 and 23 K. *J. Chem. Soc., Faraday Trans.* **90**, 3609 (1994). [doi:10.1039/ft9949003609](https://doi.org/10.1039/ft9949003609)
26. Materials and methods are available as supplementary materials on *Science Online*.
27. L. Scharfenberg, H. Haak, G. Meijer, S. Y. T. van de Meerakker, Operation of a Stark decelerator with optimum acceptance. *Phys. Rev. A* **79**, 023410 (2009). [doi:10.1103/PhysRevA.79.023410](https://doi.org/10.1103/PhysRevA.79.023410)
28. It was verified that all scattered molecules are detected with equal probability, and no density-to-flux correction was needed to relate the measured scattering signals to relative inelastic cross sections. See supplementary materials for more information.
29. L. Scharfenberg *et al.*, Scattering of Stark-decelerated OH radicals with rare-gas atoms. *Eur. Phys. J. D* **65**, 189 (2011). [doi:10.1140/epjd/e2011-20009-4](https://doi.org/10.1140/epjd/e2011-20009-4)
30. P. J. Dagdigian, M. H. Alexander, Tensor cross sections and the collisional evolution of state multipoles: OH( $X(2\Pi)$ )-Ar. *J. Chem. Phys.* **130**, 094303 (2009). [doi:10.1063/1.3078386](https://doi.org/10.1063/1.3078386) [Medline](#)

31. M. T. Nguyen, R. Sumathi, D. Sengupta, J. Peeters, Theoretical analysis of reactions related to the HNO<sub>2</sub> energy surface: OH + NO and H + NO<sub>2</sub>. *Chem. Phys.* **230**, 1 (1998). [doi:10.1016/S0301-0104\(97\)00383-2](https://doi.org/10.1016/S0301-0104(97)00383-2)
32. The OH-NO spin states with  $S = 0$  and  $S = 1$  are not distinguished in our model; the  $4 \times 4$  matrices for each spin state are therefore identical.
33. Although the quadrupole moment vanishes in the  $j = 1/2$  state of NO, the quadrupole moment in the molecular frame contributes to the collisions producing NO states with  $j = 3/2$  and  $5/2$  that yield important contributions to the measured cross sections.
34. G. C. Groenenboom, A. V. Fishchuk, A. van der Avoird, Bound states of the OH(2Pi)-HCl complex on ab initio diabatic potentials. *J. Chem. Phys.* **131**, 124307 (2009). [doi:10.1063/1.3123426](https://doi.org/10.1063/1.3123426) [Medline](#)
35. A. van der Avoird, P. E. S. Wormer, F. Mulder, R. M. Berns, Ab initio studies of the interactions in Van der Waals molecules. *Top. Curr. Chem.* **93**, 1 (1980). [doi:10.1007/3-540-10058-X\\_7](https://doi.org/10.1007/3-540-10058-X_7)
36. H.-J. Werner, P. J. Knowles, An efficient internally contracted multiconfiguration-reference configuration interaction method. *J. Chem. Phys.* **89**, 5803 (1988). [doi:10.1063/1.455556](https://doi.org/10.1063/1.455556)
37. T. H. Dunning, Gaussian basis sets for use in correlated molecular calculations. I. The atoms boron through neon and hydrogen. *J. Chem. Phys.* **90**, 1007 (1989). [doi:10.1063/1.456153](https://doi.org/10.1063/1.456153)
38. MOLPRO, A package of ab initio programs, H.-J. Werner, P. J. Knowles, R. Lindh, F. R. Manby, M. Schütz *et al.*; see <http://www.molpro.net>.
39. J. P. Maillard, J. Chauville, A. W. Mantz, High-resolution emission spectrum of OH in an oxyacetylene flame from 3.7 to 0.9  $\mu\text{m}$ . *J. Mol. Spectrosc.* **63**, 120 (1976). [doi:10.1016/0022-2852\(67\)90139-7](https://doi.org/10.1016/0022-2852(67)90139-7)
40. J. W. C. Johns, J. Reid, D. W. Leppard, The vibration-rotation fundamental of NO. *J. Mol. Spectrosc.* **65**, 155 (1977). [doi:10.1016/0022-2852\(77\)90368-X](https://doi.org/10.1016/0022-2852(77)90368-X)
41. D. J. Margoliash, W. J. Meath, Pseudospectral dipole oscillator strength distributions and some related two body interaction coefficients for H, He, Li, N, O, H<sub>2</sub>, N<sub>2</sub>, O<sub>2</sub>, NO, N<sub>2</sub>O, H<sub>2</sub>O, NH<sub>3</sub>, and CH<sub>4</sub>. *J. Chem. Phys.* **68**, 1426 (1978). [doi:10.1063/1.435963](https://doi.org/10.1063/1.435963)
42. D. Spelsberg, Dynamic multipole polarizabilities and reduced spectra for OH, application to the long-range part of the two lowest potential surfaces of the OH-CO complex. *J. Chem. Phys.* **111**, 9625 (1999). [doi:10.1063/1.480295](https://doi.org/10.1063/1.480295)
43. K. T. Tang, J. P. Toennies, An improved simple model for the van der Waals potential based on universal damping functions for the dispersion coefficients. *J. Chem. Phys.* **80**, 3726 (1984). [doi:10.1063/1.447150](https://doi.org/10.1063/1.447150)
44. B. R. Johnson, The renormalized Numerov method applied to calculating bound states of the coupled-channel Schroedinger equation. *J. Chem. Phys.* **69**, 4678 (1978). [doi:10.1063/1.436421](https://doi.org/10.1063/1.436421)
45. B. R. Johnson, *NRCC Proceedings* **5**, 86 (1979).

46. D. M. Sonnenfroh, K. Liu, Number density-to-flux transformation revisited: Kinematic effects in the use of laser-induced fluorescence for scattering experiments. *Chem. Phys. Lett.* **176**, 183 (1991). [doi:10.1016/0009-2614\(91\)90152-Y](https://doi.org/10.1016/0009-2614(91)90152-Y)
47. Ch. Naulin, M. Costes, A. Benseddik, G. Dorthe, Kinematic effects on laser-induced fluorescence measurements performed in reactive crossed beam experiments. *Laser Chem.* **8**, 283 (1988). [doi:10.1155/LC.8.283](https://doi.org/10.1155/LC.8.283)
48. M. Kirste *et al.*, Communication: Magnetic dipole transitions in the OH A  $2\Sigma^+ \leftarrow X^2\Pi$  system. *J. Chem. Phys.* **137**, 101102 (2012). [doi:10.1063/1.4751475](https://doi.org/10.1063/1.4751475) [Medline](#)
49. C. D. Ball, F. C. De Lucia, Direct observation of  $\Lambda$ -doublet and hyperfine branching ratios for rotationally inelastic collisions of NO–He at 4.2 K. *Chem. Phys. Lett.* **300**, 227 (1999). [doi:10.1016/S0009-2614\(98\)01328-1](https://doi.org/10.1016/S0009-2614(98)01328-1)